

Chapter 8

Nb₃Sn 11 T Dipole for the High Luminosity LHC (FNAL)



Alexander V. Zlobin

Abstract This chapter describes the design and parameters of the 11 T dipole developed at the Fermi National Accelerator Laboratory (FNAL) in collaboration with the European Organization for Nuclear Research (CERN) for the High Luminosity LHC project, and presents details of the single-aperture and twin-aperture dipole models that were constructed and tested. Magnet test results including magnet quench performance, magnetic measurements, and quench protection studies performed using the dipole mirror and single-aperture and twin-aperture dipole models are summarized and discussed.

8.1 Introduction

The operation of the Large Hadron Collider (LHC) at higher luminosities requires the installation of additional collimators in the dispersion suppression (DS) regions (Bottura et al. 2012; de Rijk et al. 2010) (see also Chap. 9). The free warm longitudinal space of ~ 3.5 m that is required for additional collimators can be provided by substituting some regular 14.3 m long 8.33 T LHC main dipoles (MB) with a pair of 5.5 m long 11 T dipoles (Bottura et al. 2012). These twin-aperture dipoles will operate at 1.9 K in series with the main dipoles, and deliver the same integrated strength of 119 T m at a nominal operating current of 11.85 kA. The operating field level of ~ 11 T calls for magnets based on Nb₃Sn superconductor.

To demonstrate feasibility of such magnets and study their performance parameters, in 2011 the European Organization for Nuclear Research (CERN) and the Fermi National Accelerator Laboratory (FNAL) started a research and development (R&D) program with the goal of developing and testing a 5.5 m long twin-aperture

A. V. Zlobin (✉)

Fermi National Accelerator Laboratory (FNAL), Batavia, IL, USA

e-mail: zlobin@fnal.gov

© The Author(s) 2019

D. Schoerling, A. V. Zlobin (eds.), *Nb₃Sn Accelerator Magnets*, Particle Acceleration and Detection, https://doi.org/10.1007/978-3-030-16118-7_8

This manuscript has been authored by Fermi Research Alliance, LLC under Contract No. DE-AC02-07CH11359 with the U.S. Department of Energy, Office of Science, Office of High Energy Physics.

Nb₃Sn dipole prototype. The original FNAL–CERN R&D plan comprised three phases:

- Phase 1 (2011–2012): development and testing of a single-aperture 2 m long dipole demonstrator, first at FNAL and then, after technology transfer, at CERN;
- Phase 2 (2013–2014): development and testing of two 2 m long twin-aperture dipole models at each laboratory to study the magnets' performance parameters and their reproducibility, and to select the magnet's final design;
- Phase 3 (2014–2015): development and testing of a 5.5 m long twin-aperture dipole prototype to demonstrate the technology scale-up and production readiness. It was assumed that one 5.5 m long collared coil would be produced by FNAL and the other one by CERN.

In 2013 the FNAL plan was modified due to the reduction of the FNAL program budget as well as CERN's priorities and the schedule for US contributions to the LHC Luminosity Upgrade (HL-LHC) project. In the new plan the third phase of the FNAL plan was cancelled, and the scope of the second phase was modified. The model length was reduced from 2 m to 1 m, to minimize the magnet cost.

The design and technology of the 11 T dipole was influenced by the design of the LHC Nb-Ti main dipole and by the results of the Nb₃Sn magnet R&D program at FNAL (Zlobin 2010) (see also Chap. 7). To meet the tight project schedule within the available budget, the magnet was designed to make maximum use of the existing tooling, infrastructure, and magnet components at both laboratories.

8.2 Magnet Design Concept

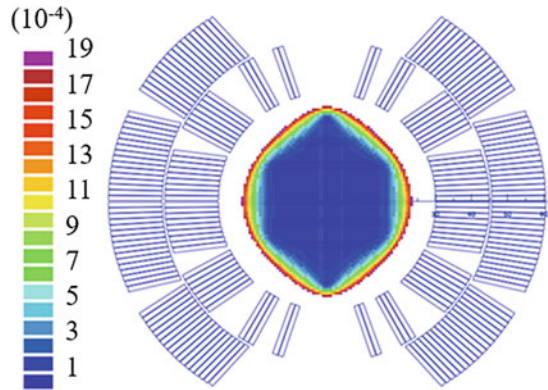
8.2.1 Design Considerations

The main design goals included achieving a dipole field above 11 T at a current of 11.85 kA with 20% margin on the load line at an operating temperature of 1.9 K, and providing geometrical field harmonics below the 10^{-4} level at the reference radius of 17 mm (Karppinen et al. 2012; Zlobin et al. 2011).

The design concept for the 11 T dipole features a two-layer shell-type coil, stainless-steel collars, and a vertically split iron yoke, surrounded by a stainless-steel outer shell. The 60 mm coil aperture, slightly larger than the 56 mm aperture of the LHC main dipole, was selected to accommodate the beam sagitta in the 11 T dipoles and to avoid the manufacture of curved Nb₃Sn coils. The aperture separation is 194 mm, as in the LHC main dipole. The size and location of the heat-exchanger and the slots for the bus-bars inside the iron yoke of the 11 T dipole are identical to those of the MB yoke.

The parameters of the Nb₃Sn Rutherford cable were selected using the following considerations. The maximum number of strands in the cable was limited to 40 by

Fig. 8.1 Coil cross-section with geometrical field errors in units



the capability of CERN's cabling machine (FNAL cabling machine allows for 42 strands). The maximum strand diameter was restricted by 0.7 mm to limit the cable thickness and, thus, to achieve the required field of 11 T or more at the nominal current of 11.85 kA. The acceptable critical current degradation due to cabling was limited to 10%. Magnet design studies started with the following cable geometrical parameters: a width of 14.85 mm, a thin edge of 1.20 mm, a thick edge of 1.41 mm, and a keystone angle of 0.81° . The cable insulation thickness was 0.1 mm.

Several two-layer coil cross-sections with five, six, and seven blocks per quadrant and 60 mm aperture were analyzed using the ROXIE program (Russenschuck 1995). A six-block design with 56 turns, which satisfied the above criteria, was selected for further optimization. A cross-section of this coil, optimized for the twin-aperture layout with a round iron yoke separated from the coil by 30 mm, is shown in Fig. 8.1.

To simplify the magnet assembly and reduce the risk of coil damage during collaring, it was decided to use separate collars for each aperture. An additional advantage of this approach is the possibility of testing collared coils in both single-aperture and twin-aperture configurations. The collar width in this magnet is limited to 30 mm by the available space between the two apertures. This space is not enough for using a freestanding collar design. With support from the yoke and skin, however, the collar width can be less than 30 mm. The minimum collar width that satisfies the stress limits in the collar and key materials is about 20 mm.

Analysis of the stress distribution in the coil showed that during collaring the stress in the coil pole regions is significantly smaller than the stress in the mid-plane regions due to the relatively large width and high rigidity of the coil. The low pre-stress in the pole region, limited by the maximum allowed stress in the coil mid-plane during collaring, can be increased to the required level by coil bending using the mid-plane collar–yoke shim or by using removable poles with shims. Both methods were adopted for the mechanical structure of the 11 T dipole. CERN focused on the removable pole design and wide round collar, whereas FNAL pursued the integrated pole design and a narrower elliptical collar to provide coil bending. The results of magnetic and mechanical analyses for the FNAL 11 T dipole

models are presented in Auchmann et al. (2012), Karppinen et al. (2012), and Zlobin et al. (2012a).

8.2.2 Mechanical Designs and Analysis

The integrated pole design approach stands upon previous FNAL experience with Nb_3Sn dipole and quadrupole coils. Cross-sections of the collared coil and the 11 T single-aperture and twin-aperture dipoles that were developed at FNAL are shown in Figs. 8.2 and 8.3.

The collar has a slightly elliptical shape, with a minimum width in the mid-plane of 25 mm. In the single-aperture configuration, the collared coil is placed inside the 400 mm diameter iron yoke used previously in FNAL HFDA series dipole models (see Chap. 7). The inner contour of the yoke was adapted to the collared coil design. The two yoke halves are connected by Al clamps and a 12 mm thick stainless-steel skin. In the twin-aperture configuration, two collared coils, separated by an iron

Fig. 8.2 Collared coil cross-section

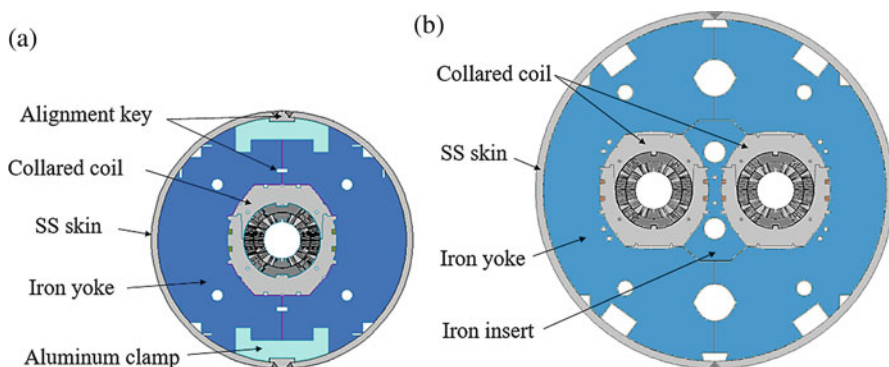
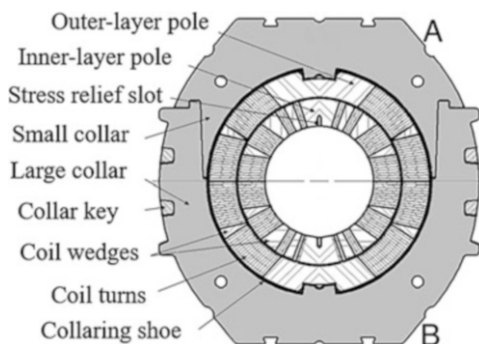


Fig. 8.3 (a) Single-aperture and (b) twin-aperture dipole cross-sections

insert, are placed inside the 550 mm diameter iron yoke between the two yoke pieces surrounded by a 12 mm thick stainless-steel skin.

The required coil pre-stress is applied in several steps. The initial coil preloading is provided by adding 0.1 mm mid-plane (or by using coils with a 0.1 mm larger azimuthal size) and 0.025 mm radial shims during the collaring of the coils. The maximum achievable pre-stress in the pole region is limited at this stage by the maximum allowed stress near the coil mid-plane. During cold mass assembly the coil pole pre-stress is increased to the nominal level by the horizontal deformation of the collared coil, using 0.125 mm horizontal collar–yoke shims. These shims also provide the collar–yoke contact in the mid-plane area after cool-down.

The vertical gap between the two yoke halves is open at room temperature. It is controlled by the precise collar dimensions near the top and bottom horizontal surfaces of the collared coil (areas A and B in Fig. 8.2). Due to the larger thermal contraction of the outer shell, the clamps, and the collared coil relative to the iron yoke, the gap is closed during the cool-down to 1.9 K, and compressed by the shell and clamps to stay closed up to the maximum design field of 12 T. The maximum tensile stress in the 12 mm thick stainless-steel shell is approximately 250 MPa. This large shell stress increases the compression of the iron halves with very small impact on the coil preload.

A detailed mechanical analysis was performed to optimize the stress in the coil and major elements of the magnet support structure, and to minimize the conductor motion and coil cross-section deformation at room and operating temperatures. Stress distribution diagrams for the coil in twin-aperture configuration are shown in Fig. 8.4.

The values for the maximum compressive coil stress in the pole and mid-plane turns during assembly and operation for the twin-aperture and single-aperture magnets are summarized in Table 8.1. In both cases the poles remain under compression at all steps, and the maximum coil stress remains below 165 MPa.

The maximum stress values for the major elements of the magnet support structure at different assembly and operating stages are below the yield stress of the structural materials chosen. The maximum radial deflection of the coil cross-section with respect to the magnet's nominal design decreases from 0.135 mm at injection current to less than 0.04 mm at the nominal current, which is acceptable.

8.2.3 Magnetic Design and Analysis

The main challenges for the electromagnetic design of the twin-aperture 11 T dipole include matching the transfer function (TF) of the main LHC dipoles, controlling the magnetic coupling of the two apertures, and minimizing the level and variation of unwanted multipoles in the operating field range. Iron saturation and coil

Fig. 8.4 Distributions of the azimuthal stress in the coil for twin-aperture configuration: (a) after assembly; (b) after cool-down; and (c) at 12 T

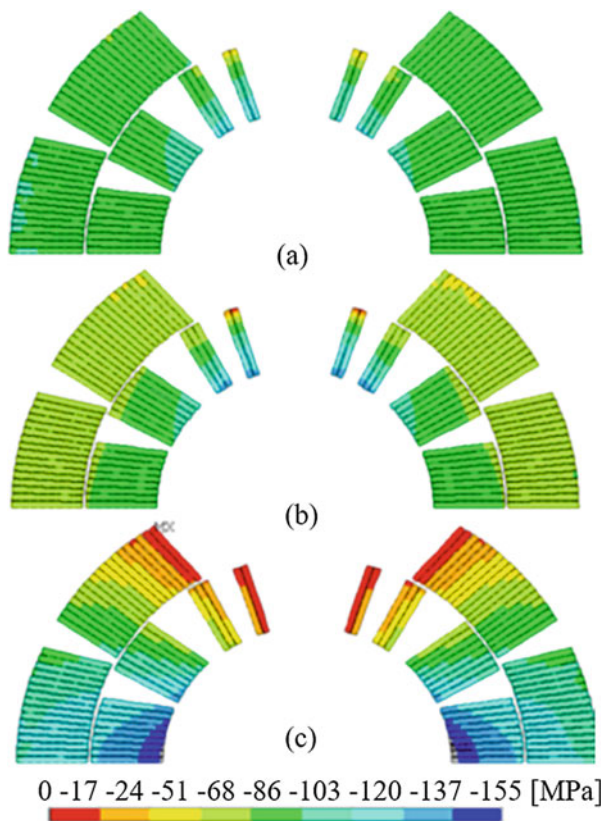


Table 8.1 Maximum compressive azimuthal stress in coil pole and mid-plane turns (MPa). The data in parentheses corresponds to the single-aperture design

Position in coil	Collared coil	Cold mass	Cool-down	Design field 12 T
Inner-layer pole	47 (44)	103 (120)	117 (136)	5 (2)
Outer-layer pole	81 (64)	85 (87)	59 (110)	25 (17)
Inner-layer mid-plane	117 (97)	77 (79)	80 (97)	165 (141)
Outer-layer mid-plane	59 (51)	85 (108)	66 (124)	116 (153)

magnetization are the two most important effects that contribute to the TF and low-order field harmonics. Both effects are non-linear, which makes their compensation rather challenging.

Field harmonic coefficients in a magnet aperture are defined as

Table 8.2 Transfer function and field harmonics (in units) at $R_{\text{ref}} = 17$ mm

Parameter	Twin-aperture		Single-aperture	
	0.757 kA	11.85 kA	0.757 kA	11.85 kA
B_1/I (T/kA)	1.01	0.95	1.01	0.92
b_2	0.13	-7.14	-	-
b_3	44.51	6.04	38.4	-0.8
b_4	0.05	-0.44	-	-
b_5	0.01	-0.02	5.3	0.1
b_7	0.04	0.02	0.0	0.0
b_9	0.19	0.96	1.0	1.0

$$B_y + iB_x = B_1 \sum_{n=1}^{\infty} (b_n + ia_n) \left(\frac{x + iy}{R_{\text{ref}}} \right)^{n-1},$$

where B_x and B_y are the horizontal and vertical field components, and b_n and a_n are the $2n$ -pole normal and skew harmonic coefficients at the reference radius $R_{\text{ref}} = 17$ mm. The normal b_n and skew a_n harmonic coefficients are expressed in units of 10^{-4} parts of the main dipole field B_1 .

Table 8.2 shows the magnet TF, defined as the ratio B_1/I , and the allowed low-order field harmonics b_n calculated for the magnet's straight section of the twin-aperture and single-aperture 11 T dipoles at an injection current of 757 A and at a nominal current of 11.85 kA. The LHC current pre-cycle with a minimal (reset) current of 350 A was used. The data include geometrical components and the contributions from the coil magnetization and iron saturation effects.

The iron saturation influences the magnet's TF and the low-order field harmonics b_2 , b_3 , and b_5 . Due to this effect, the TF of the twin-aperture model is reduced by 6%. Two large holes in the yoke insert (see Fig. 8.3) were added to limit the b_2 variation by 11 units. The cut-outs above and below the collared coils, the size and position of the small holes around the collared coils, and the location of the holes for tie-rods in Fig. 8.3 were used to keep the b_3 and b_5 variations from injection to a nominal current below 0.1 unit. The iron cross-section of the single-aperture models was not optimized to suppress the iron saturation effect. Thus, the TF reduction in the single-aperture design reaches 9%, and the b_5 variation increases to 1.3 units.

The coil magnetization effect in the 11 T Nb₃Sn dipoles is much larger than in the Nb-Ti LHC MB dipoles due to the higher critical current density and the larger size of the superconducting filaments in the state-of-the-art Nb₃Sn composite wires. Beam dynamics studies have shown that b_3 errors of up to ± 20 units at injection can be tolerated without compromising the LHC's dynamic aperture. The calculated b_3 due to the persistent currents in the 11 T dipole is ~ 44 units at the LHC injection current. Analysis has shown that the b_3 variations in the operating field range could be limited to ± 20 units by reducing the LHC reset current to 100 A. Possible passive correction schemes were also studied to further reduce b_3 at low fields (Auchmann et al. 2012).

Table 8.3 Dipole design parameters at $I_{\text{nom}} = 11.85$ kA

Parameter	Twin-aperture	Single-aperture
Yoke outer diameter (mm)	550	400
Nominal bore field at I_{nom} (T)	11.23	10.88 (11.07) ^a
Short sample field B_{SSL} at T_{op} (T)	13.9	13.4 (14.1) ^a
Margin $B_{\text{nom}}/B_{\text{SSL}}$ at T_{op} (%)	83	81 (79) ^a
Stored energy at I_{nom} (kJ/m)	969	424 (445) ^a
F_x /quadrant at I_{nom} (MN/m)	3.16	2.89
F_y /quadrant at I_{nom} (MN/m)	-1.59	-1.58

^a1 m long model

8.2.4 Magnet Design Parameters

The 2D calculated design parameters for the twin-aperture and single-aperture dipole magnets at a nominal operating current of 11.85 kA and a temperature of 1.9 K are presented in Table 8.3. The calculation was performed for a wire J_c (12 T, 4.2 K) of 2750 A/mm^2 , a Cu fraction of 0.53, and a cable I_c degradation of 10%. In the single-aperture configuration the calculated nominal central field is 10.88 T, whereas in the twin-aperture magnet it increases to 11.23 T due to field enhancement in the twin-aperture configuration. For a 1 m long model the nominal and short sample bore fields are also slightly larger due to contributions to the central field from the coil ends.

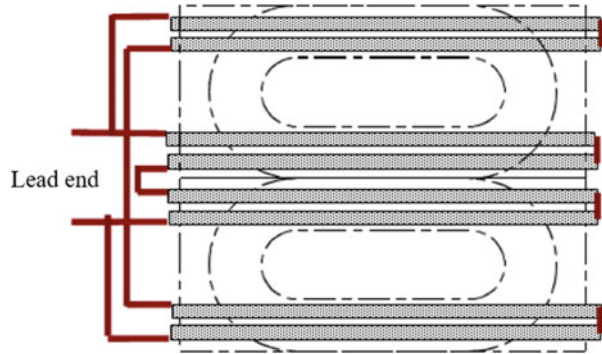
8.2.5 Quench Protection

The 11 T Nb₃Sn dipoles have a larger stored energy and inductance per unit length than the main LHC dipoles and, thus, require special attention to their protection during a quench. The preliminary quench analysis suggested that the quench protection scheme with efficient outer-layer (OL) heaters could provide adequate protection for the 11 T Nb₃Sn dipoles. The quench protection heaters are made of stainless-steel strips and placed on the coils' outer surface. The heater strips on one side of each coil are connected in series with the strips on the same side of the other coil, forming two symmetric heater circuits (see Fig. 8.5). The two circuits are connected in parallel for redundancy.

In the case of a magnet quench at the maximum operating current of 11.85 kA, the expected average temperature of the coil OL under the heaters is less than 140 K when both heater circuits operate, and less than 200 K in the case of one heater circuit failure. The maximum hot-spot temperature calculated for a 50 ms protection system delay does not exceed 240 K and 340 K, respectively.

Reliable quench protection for the 11 T dipoles with OL heaters requires high heater efficiency. Experimental studies and optimization of the protection heaters were a key part of the 11 T dipole R&D program at FNAL.

Fig. 8.5 Electrical connection of protection heaters



8.3 11 T Dipole R&D

8.3.1 Model Design and Fabrication

The 11 T dipole R&D at FNAL started with the development of the baseline technology and tooling, and the optimization of strand and cable parameters. The strand and cable parameters are the same for both the FNAL and CERN dipole designs. The design of the FNAL dipole including coil, collar, and iron yoke, as well as magnet assembly processes and preload procedures, were developed in parallel. Experimental studies of magnet quench performance, protection, field quality, and performance reproducibility were then performed.

8.3.1.1 Nb₃Sn Wire and Cable

The 11 T dipole uses Rutherford cable with 40 Nb₃Sn strands, 0.7 mm in diameter. The optimization of cable parameters included the selection of the cable cross-section geometry and compaction to achieve a good mechanical stability of the cable and acceptable critical current degradation, incorporating a stainless-steel core and preserving a high residual resistivity ratio (RRR) of the copper matrix. Two strand designs (baseline and R&D) with a different sub-element number, size, and distribution in the cross-section were used. The cross-sections of the round wires and the cored cable are shown in Fig. 8.6.

The main parameters and properties of the Nb₃Sn wires and Rutherford cables are discussed in Chap. 2 of this book. Results of the wire and cable study and optimization for the 11 T program at FNAL are reported by Barzi et al. (2012). The Nb₃Sn wires were produced using the Restack Rod Process[®] (RRP) by Oxford Superconducting Technologies (OST). The main parameters of RRP108/127 (baseline) and RRP150/169 (R&D) round wires are summarized in Table 8.4.

During the reaction, Nb₃Sn strands expand due to the phase transformation. The 11 T dipole cable measured in free conditions showed an average width expansion of

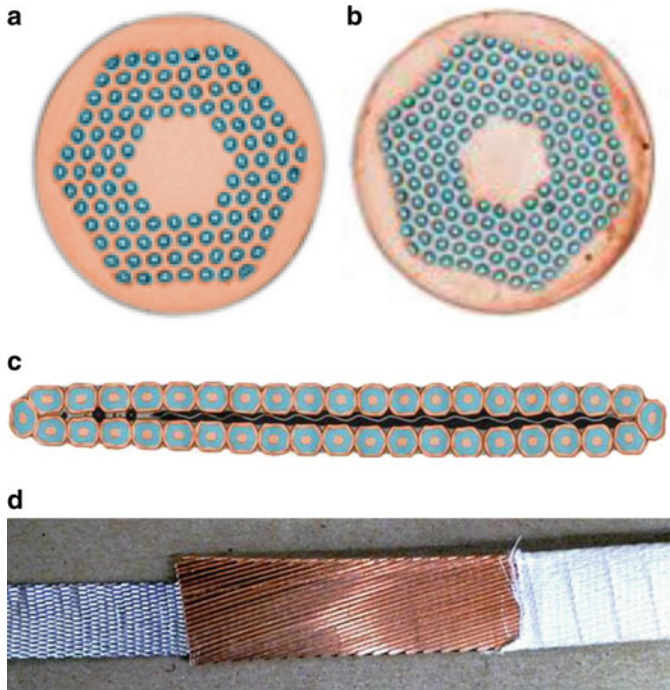


Fig. 8.6 (a) RRP108/127 and (b) RRP150/169 composite wires; (c) the 40-strand Rutherford cable with stainless-steel core; and (d) the cored cable insulated with E-glass tape

Table 8.4 Nb₃Sn round wire parameters

Parameter	RRP108/127	RRP150/169
Strand diameters (mm)	0.70	0.70
Average $J_c(12\text{ T}, 4.2\text{ K})$ (kA/mm ²)	2.68	2.65
Effective filament size D_{eff} (μm)	41	36
Twist pitch (mm)	14	13
Cu fraction (%)	55.5	51.8

Table 8.5 Cable geometrical parameters

Parameter	Un-reacted	Reacted
Mid-thickness (mm)	1.25	1.30
Thin edge (mm)	1.15	1.19
Thick edge (mm)	1.35	1.40
Width (mm)	14.70	15.08
Keystone angle ($^\circ$)	0.79	0.81

2.6%, an average mid-thickness expansion of 3.9%, and an average length decrease of 0.3%. An explanation of the anisotropic cable expansion is presented by Andreev et al. (2002). The geometrical parameters of the un-reacted and reacted cable

optimized for the 11 T dipole are listed in Table 8.5. The geometrical parameters of the coil winding and curing tooling are determined by the un-reacted cable cross-section, whereas the geometrical parameters of the coil reaction and impregnation tooling are based on the reacted cable dimensions. The latter were also used for the magnet's electromagnetic and structural optimization. Cable samples with and without a stainless-steel core were fabricated and tested at FNAL. Based on the experimental data, the critical current degradation from cabling after optimization was less than 4%.

8.3.1.2 Coil

Each coil consists of two layers and 56 turns. The coil is wound from a single piece of cable insulated with two layers of E-glass tape 0.075 mm thick and 12.7 mm wide (see Fig. 8.6d). This insulation is adequate for the R&D phase. The final cable insulation was selected and tested in the framework of the CERN 11 T program (see Chap. 9). The cable layer jump is integrated into the lead end-spacers. Both coil poles were made of Ti-6Al-4 V alloy, whereas the wedges, end-spacers, and saddles were made of stainless steel. The end-spacers were fabricated using the selective laser sintering (SLS) process and provided by CERN for all FNAL coils.

Coils are fabricated using the wind-and-react method, i.e., the superconducting Nb₃Sn phase is formed during the coil high-temperature heat treatment. The details of the coil fabrication process are reported by Zlobin et al. (2012a, 2013). After winding, each coil layer was impregnated with CTD-1202x liquid ceramic binder and cured under a small pressure at 150 °C for 0.5 h. During curing the coil inner and outer layers were shimmed in the mid-plane to a size of 1.0 and 1.5 mm, respectively, smaller than the layer nominal sizes, to provide room for the Nb₃Sn cable volume's expansion after reaction. Each coil was reacted separately in an argon atmosphere using a three-step cycle. The maximum temperature for coils with RRP108/127 wires was 640 °C for 48 h (HT1); for the last two coils (11 and 12) it was increased to 645 °C for 50 h (HT2). The coils with RRP150/169 wires were reacted at 665 °C for 50 h (HT3). Before impregnation, the brittle Nb₃Sn coil leads were spliced to flexible Nb-Ti cables, and the coils were wrapped with a 0.125 mm thick layer of E-glass or S2-glass cloth. The coils were impregnated with CTD-101K epoxy and cured at 125 °C for 21 h. Pictures of a coil after curing, reaction, and impregnation, and a coil cross-section are shown in Fig. 8.7.

The radial and azimuthal sizes of each coil were measured in free condition in several cross-sections using a 3D Cordax machine. An example of the coil size measurements is shown in Fig. 8.8. One can see that the coil outer radius is smaller than nominal by ~0.05 mm. This difference was compensated for during magnet assembly by adding an appropriate layer of Kapton film. An oversizing of the coil mid-plane by ~0.1 mm was introduced to achieve the target coil pre-stress without using special mid-plane shims. It was found that the radial and azimuthal sizes of impregnated coils are reproducible from coil to coil. Thus, they can be adjusted using appropriate radial and azimuthal shims in the impregnation mold.

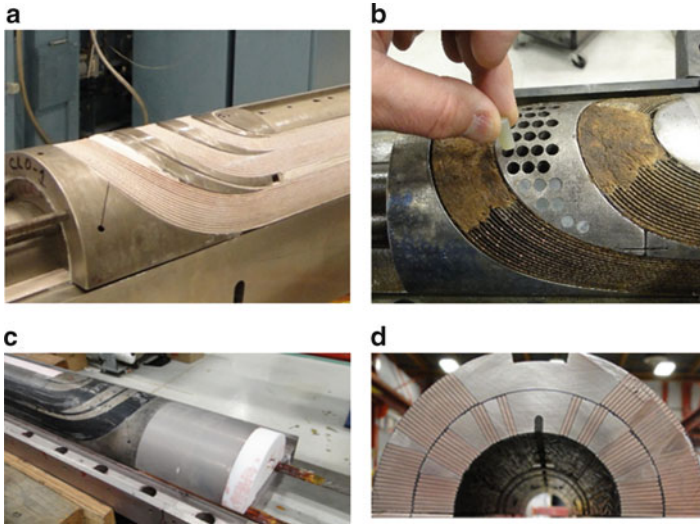


Fig. 8.7 (a) Coil after winding and curing (lead end); (b) reacted coil with v.3 end-spacers (G10 plugs are inserted in special holes in end spacers before impregnation); (c) epoxy impregnated coil and splice block; (d) coil cross-section illustrating the accuracy of the turn and spacer positions

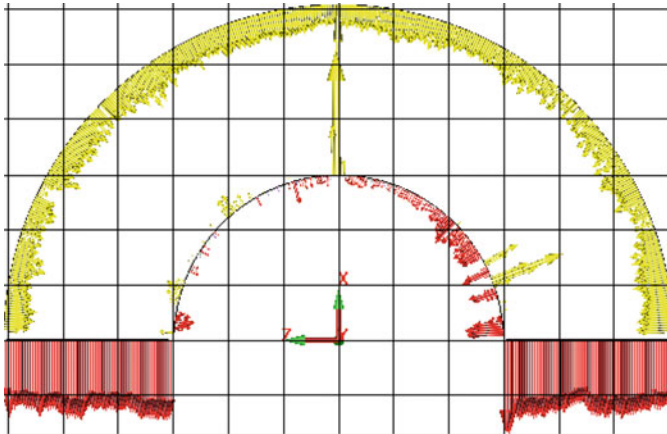
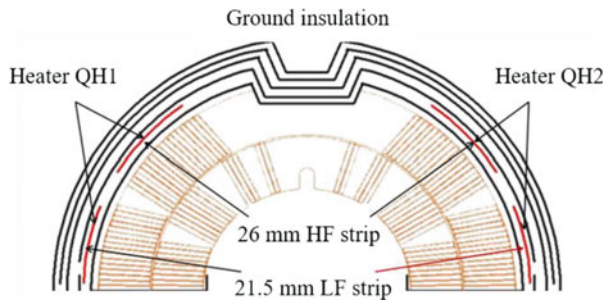


Fig. 8.8 Example of coil size measurements (coil 10). The side of each square corresponds to 0.1 mm

Four 2 m long and eight 1 m long coils were fabricated at FNAL during 2012–2014 using various wires, cables, coil end parts, and reaction cycles. Three end-spacer designs were used: the original design (v.1), the design with shortened legs (v.2), and the design with flexible legs and round holes (v.3) filled with

Table 8.6 Coil design features

Coil number	Length (m)	Strand design	Cable core	End-spacers	Reaction cycle
1 ^a	2	108/127	No	v.1	HT1
2, 3, 4 ^b	2	108/127	No	v.1	HT1
5, 6 ^b , 7	1	150/169	Yes	v.1	HT3
8	1	108/127	Yes	v.1	HT1
9, 10	1	108/127	Yes	v.2	HT1
11, 12	1	108/127	Yes	v.3	HT2

^aPractice coil^bCoil damaged during fabrication**Fig. 8.9** Position of high-field (HF) and low-field (LF) protection heaters

G10 rods after reaction (see Fig. 8.7b). Coil design features are summarized in Table 8.6.

8.3.1.3 Ground Insulation and Quench Protection Heaters

The coil ground insulation consists of five layers of 0.125 mm thick polyimide film. Two quench protection heaters made of 0.025 mm thick stainless-steel strips are placed on each side of the coil between the first and second insulation layers, covering the OL coil blocks (Fig. 8.9). The resistance of each heater at 300 K is 5.9 Ω. The corresponding strips on each side of each coil are connected in series forming two independent heaters, as shown in Fig. 8.5.

8.3.1.4 Collared Coil

The collared coil assembly consists of two coils, a multilayer polyimide ground insulation, 316 L stainless-steel protection shells (collaring shoe), and collar laminations made of Nirosta high-Mn stainless steel. Collar blocks are locked on each side by two bronze keys. The models were assembled first with laser-cut collars (v.1) and later with stamped collars (v.2). The stamped collars had a slightly larger inner radius to accommodate a thicker protective shell.

Assembly and preload procedures for brittle Nb_3Sn coils with a collar structure were developed and successfully demonstrated at FNAL using quadrupole coils (Bossert et al. 2011). Since the collaring of Nb_3Sn coils always requires great care and process control, a 0.6 m long mechanical model with instrumented Nb_3Sn coils was assembled and used to optimize these procedures, as well as the coil final preload.

8.3.1.5 Short Dipole Models

Single-Aperture Models

In the single-aperture configuration, a collared coil is installed inside a vertically split yoke of 400 mm outer diameter made of SAE 1045 iron and fixed with Al clamps similar to the HFDA series dipoles (see Chap. 7). The collared coil inside the iron yoke is shown in Fig. 8.10. To assure uniform mechanical support of the collared coil, the yoke covers the entire coil length, including the $\text{Nb}_3\text{Sn}/\text{Nb-Ti}$ lead splices. In this case, the maximum field in the coil ends is $\sim 2\%$ higher than the maximum field in the coil straight section.

The 12.7 mm thick 304 L stainless-steel skin is pre-tensioned during welding (welded skin) or by strong bolts (bolted skin) to provide the coil's final pre-compression. The required minimal stress in the skin at room temperature was

Fig. 8.10 Collared coil with collar-yoke shims inside iron yoke (lead end)



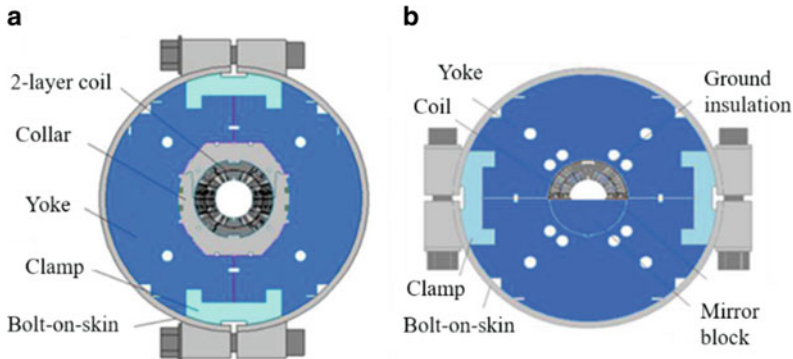


Fig. 8.11 Cross-sections of (a) 11 T dipole and (b) dipole mirror with a bolted skin

controlled using the data from strain gauges installed on the skin. Two 50 mm thick 304 L stainless-steel end-plates are attached to the shell to restrict the axial motion of the coil ends.

Some single 11 T dipole coils were tested using the dipole mirror structure and assembly procedure developed for the HFDM series (see Chap. 7). Due to the larger radial size of the 11 T coils, the 8 mm thick radial bronze spacer in HFDM structure was replaced by a 2 mm thick stainless-steel shell. Cross-sections of the single-aperture 11 T dipole and dipole mirror models with bolted skin are shown in Fig. 8.11.

The 11 T dipole demonstrator MBHSP01 used 2 m long coils 2 and 3. Single-aperture dipole models MBHSP02 and MBHSP03 used 1 m long coils 5, 7, 9, and 10. Coil 8 was heavily instrumented and was first tested in the dipole mirror model MBHSM01 to study the effect of coil pre-stress and to measure quench protection parameters (Zlobin et al. 2014). It was then assembled with coil 11 and tested in a single-aperture dipole MBHSP04 without collars, using the dipole mirror structure. Coil 11 was later tested again in the dipole mirror MBHSM02.

Twin-Aperture Model

In a twin-aperture configuration, two collared coils are placed inside a vertically split 550 mm outer diameter (OD) iron yoke with an iron spacer between them. The yoke is surrounded by a 12.7 mm thick welded stainless-steel skin. Two 50 mm thick stainless-steel end-plates, welded to the skin, restrict the axial motion of both collared coils. No axial pre-stress was applied to the coil ends.

The twin-aperture dipole model MBHDP01 was assembled using collared coils that were previously tested in MBHSP02 and MBHSP03. Based on the test results in a single-aperture configuration, the MBHSP03 collared coil was re-collared with a slightly larger radial coil-collar shim to increase the coil pre-stress. Both collared coils were installed inside the MBHDP01 iron yoke with the same collar-yoke mid-plane shims as in MBHSP03. These shims provided a collared coil bending

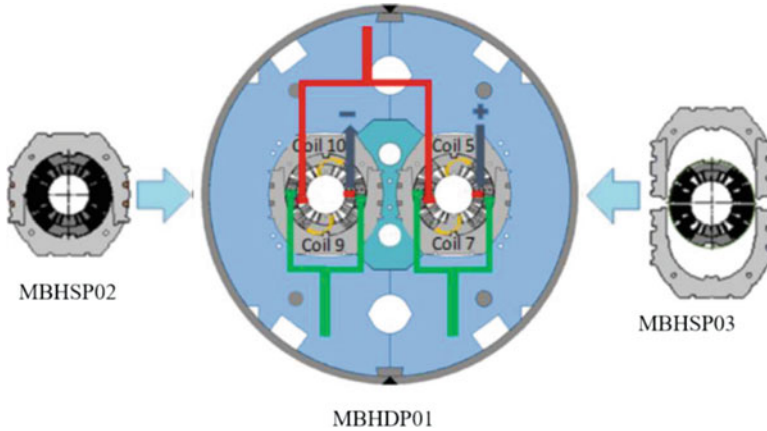


Fig. 8.12 MBHDP01 assembly and coil electrical connection schemes

of ~ 0.1 mm to ensure collar–yoke contact after cooling down. Figure 8.12 shows the twin-aperture dipole MBHDP01 assembly and the coil electrical connection scheme.

8.3.2 Magnet Test

The design features and test dates of the single-aperture dipole and dipole mirror models, and twin-aperture dipole model are summarized in Table 8.7.

All the models were tested at the FNAL Vertical Magnet Test Facility (VMTF) during 2012–2017. The magnets were instrumented with voltage taps and a quench antenna; strain gauges on the coils, shell, and end bullets; and temperature sensors to monitor the magnet parameters during assembly and test.

The typical test plan included magnet training, measurements of the ramp rate and temperature dependencies of the magnet quench current, magnetic measurements, and protection heater studies.

8.3.2.1 Quench Performance

Single-Aperture Dipoles and Mirror Models

The training quenches of single-aperture dipole models MBHSP01–04 and dipole mirror models MBHSM01–02 are summarized in Fig. 8.13. Typically, each magnet was trained first at 4.5 K with a current ramp rate of 20 A/s. When the training was slowing down or a plateau was reached, the magnet training was continued at 1.9 K.

Table 8.7 Design features of short models

Model	Coil number	Collar design	Skin type	Test date
MBHSP01	2, 3	v.1	Welded	June–July 2012
MBHSP02	5, 7	v.1	Bolted horizontal	March 2013
MBHSM01	8	No collar	Bolted horizontal	Dec 2013–Jan 2014
MBHSP03	9, 10	v.2	Bolted vertical	April–May 2014
MBHDP01	5, 7 & 9, 10	v.1. & v.2	Welded	Feb–March 2015 (TC1) ^a
MBHSP04	8, 11	No collar	Bolted horizontal	June–July 2015
MBHDP01	5, 7 & 9, 10	v.1. & v.2	Welded	June–July 2016 (TC2) ^b
MBHSM02	11	No collar	Bolted horizontal	March–April 2017

^aThermal cycle 1

^bThermal cycle 2

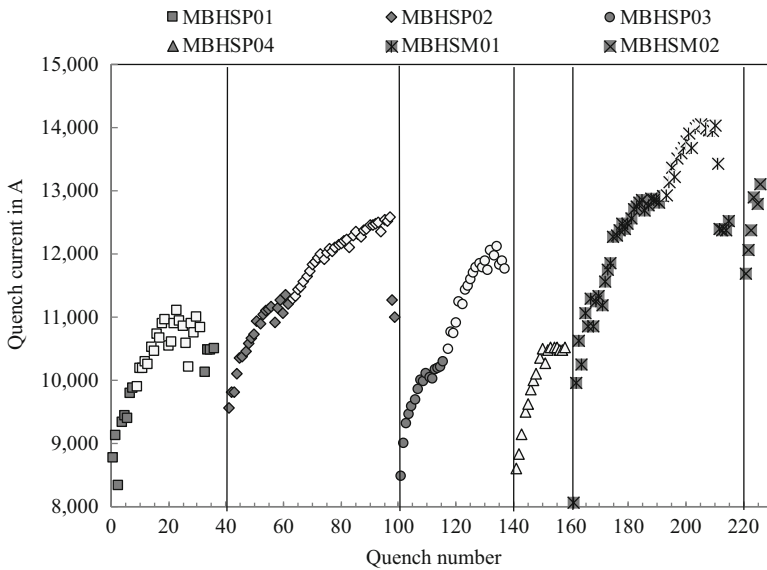


Fig. 8.13 Magnet training. The data for 4.5 K and 1.9 K are represented with filled and non-filled markers, respectively

The 2 m long, single-aperture demonstrator dipole, called MBHSP01, was tested in June–July 2012, only 18 months (!) after the start of the program. The goal of this test was to achieve the design field of 12 T and to check the magnet’s design, technology, and performance. After a first quench at ~8.2 T and 4.5 K, the magnet only reached 10.4 T, or 87% of the magnet design field of 12 T at 1.9 K. The quench performance was erratic. The magnet also spontaneously quenched after 1–6 min at constant currents above 7.5 kA (7.0 T) at 4.5 K and above 9 kA (8.4 T) at 1.9 K.

Practically all of the low ramp-rate quenches and all the quenches at constant currents at 4.5 K, 1.9 K, and intermediate temperatures started in the mid-plane block of the coil outer layer. Only a few of the first training quenches occurred in the high-field region at the very beginning of the test. The analysis of the quench location data, ramp rate, and temperature dependencies of the magnet quench current and magnet operation at a constant current pointed to conductor damage in the outer coil mid-plane area. Later, the magnet autopsy confirmed this conclusion, and indicated that this damage occurred during coil reaction and collaring. The coil end parts, collars, and coil-collar shells were modified, and the coil fabrication and magnet assembly processes of the following 1 m long models were corrected based on the lessons learned from MBHSP01.

The first 1 m long dipole model, called MBHSP02, was tested almost a year later, in March 2013. The first quench current was 9.57 kA, which corresponds to ~ 9 T in the aperture. After 17 quenches in the inner-layer (IL) end-blocks of both coils, three consequent quenches were detected in the outer mid-plane blocks of coil 7. After 23 training quenches and ramp-rate dependence studies, magnet training was continued at 1.9 K. A maximum bore field of 11.7 T (97.5% of the magnet design field but only 83% of the magnet short sample limit (SSL) bore field) was reached after 57 training quenches. At this point the magnet training at 1.9 K was discontinued. All quenches at 1.9 K occurred in the IL end-blocks of both coils. After quench studies at 1.9 K, MBHSP02 was quenched several times again at 4.6 K. These quenches at ~ 11.4 kA (10.7 T in the aperture) showed that the magnet reached the conductor limit at 4.6 K, which is only 84.3% of the magnet SSL based on witness sample data. Spontaneous quenches at constant currents were also observed in this magnet, although they occurred at higher currents, above 9 kA (8.7 T) and 11 kA (10.4 T) at 4.5 K and 1.9 K respectively, than in MBHSP01.

The unexpectedly large level of quench current degradation, as well as spontaneous quenches at a current plateau below the maximum quench current in MBHSP02, were associated with the excessive coil pre-stress and the large radial deformation of coil mid-plane areas that was used to pre-stress the coil pole turns. These issues were studied by testing a single coil in a dipole mirror structure called MBHSM01.

The dipole mirror model MBHSM01, which was assembled with smaller mid-plane shims to reduce coil pre-stress, was tested in December 2013–January 2014. The magnet was trained to 80% of its SSL after only four quenches and to almost 100% of the SSL at 4.5 and 1.9 K after 25 and 15 quenches, respectively. The coil maximum field was 12.5 T at 1.9 K and 11.6 T at 4.5 K. All training quenches started in the high-field area of the coil inner layer, with only two quenches in the coil outer layer. The quenches after reaching a training plateau at both temperatures started in the blocks, next to the IL middle wedges. Unlike MBHSP01 and MBHSP02, dipole mirror MBHSM01 demonstrated stable performance during a 25 min long current plateau (no so-called ‘holding quenches’) at 13 kA (90% of SSL) at 1.9 K and 12 kA (92% of SSL) at 4.5 K. Since the design and fabrication processes for coil 8 in MBHSM01 were the same as for coils 5 and 7 in MBHSP02, the improved quench performance of coil 8 in the dipole mirror structure suggests

that the large mid-plane collar-yoke shim was likely a major cause of the conductor degradation in the dipole model MBHSP02. This shim size in the next dipole model MBHSP03 was reduced to the level necessary to just compensate for the difference in collar and yoke thermal contraction.

The second 1 m long dipole model, called MBHSP03, with reduced coil preload, was tested in April–May 2014. Magnet training started at 4.5 K with a first quench at 8.49 kA, which corresponds to ~ 8.4 T in the aperture. After 16 quenches at 4.5 K, magnet training was continued in superfluid helium at 1.9 K. A maximum bore field of 11.6 T, which is 96.7% of the magnet design field, was reached after 35 training quenches. All of the training quenches at 1.9 K occurred in the coil IL high-field blocks. No holding quenches were detected in MBHSP03 over ~ 30 min at various steady currents up to the nominal LHC operating current of 11.85 kA. The observed variations of quench currents in MBHSP03 were likely to be due to epoxy cracking between the pole blocks and coil turns caused by the inadequate coil pre-stress. Therefore, to avoid possible conductor degradation, magnet training was discontinued.

It is interesting to note that, despite the different strand design and critical current density, and the coil pre-stress, the first 18 quenches at 4.5 K that were normalized to the corresponding magnet SSLs for both dipole models are very close. The training rates of the magnets at 1.9 K are, however, quite different. MBHSP03 (low pre-stress) was trained to 85% of its SSL bore field after 35 quenches, whereas MBHSP02 (high pre-stress) needed 65 quenches to reach 83% of its SSL bore field. Since MBHSP03 training at 1.9 K was not completed and the magnet was not quenched again at 4.5 K, it is unknown if the conductor degradation was reduced as well.

Another attempt to better understand the effect of the coil preload in the dipole structure on magnet training and degradation was made using coil 8, previously tested in the mirror structure MBHSM01, and new coil 11, which was built using modified end-spacers with flexible legs and reduced azimuthal and axial rigidity thanks to small radial holes. These two coils were assembled without collars in a dipole configuration using the dipole mirror structure with a thin stainless-steel shell between the coils and the iron yoke. The collarless dipole model MBHSP04 was tested in June–July 2015. Magnet training was only performed at 1.9 K. After 10 quenches the magnet quench current reached a stable plateau at ~ 10.5 kA (see Fig. 8.13), which corresponds to a bore field of 10.7 T. The magnet SSL at 1.9 K based on coil 8 witness sample data is 12.7 T. Thus, this magnet reached $\sim 84\%$ of its conductor limit, as did MBHSP02 and MBHSP03 with collared coils. All of the quenches were detected in the previously tested coil 8. This suggests that coil 8 could be degraded during the disassembly of MBHSM01 or during the assembly of MBHSP04.

To check if coil 11 was also degraded during MBHSP04 assembly, it was tested in the dipole mirror structure MBHSM02 in March–April 2017. The first six training quenches of this magnet at 4.5 K are shown in Fig. 8.13. One can see that coil 11 demonstrated even better performance than the virgin coil 8, confirming that it was not damaged during MBHSP04 assembly and disassembly, or during the assembly of MBHSM02.

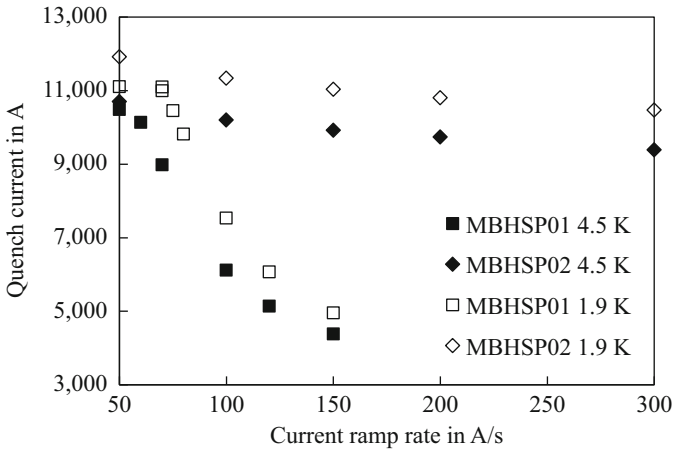


Fig. 8.14 Ramp rate dependence of magnet quench current. The data at 4.5 K and 1.9 K are represented with filled and non-filled markers, respectively

A good performance of coil 11 could be a result of its design improvements, of the new end-spacers in particular. The evaluation of the new design of end-spacers was planned by testing coils 11 and 12 in single-aperture dipole MBHSP05 (with or without collars). Due to a change of program priorities, however, this magnet was not assembled and tested.

All of the short models, except for MBHSP01, used the cable with a stainless-steel core. The positive effect of the core on the magnet ramp-rate sensitivity is shown in Fig. 8.14, where MBHSP02 ramp-rate sensitivity is compared with MBHSP01, which was made from a cable without a core.

Twin-Aperture Model

The twin-aperture dipole model MBHDP01 was tested for the first time in February–March 2015 (thermal cycle TC1). A year later, in June–July 2016, it was re-tested (thermal cycle TC2) with a new instrumentation header that permitted the installation of an anti-cryostat for magnetic measurements in one of the two apertures. The anti-cryostat with magnetic measurement probes was placed in the aperture with coils 9 and 10 used in MBHSP03.

The main goals of the MBHDP01 test were: (a) comparison of collared coil performance in single-aperture and twin-aperture configurations; (b) observation of the effect of coils 9 and 10 disassembly and re-collaring with higher pre-stress, and the effect of the smaller bending of coils 5 and 7 on magnet training and conductor degradation.

The MBHDP01 training was performed in superfluid helium at 1.9 K. Quenches occurred in all four coils, which is not surprising since the mechanical stress was changed in both collared coils. The values of the bore field in MBHDP01 and, for comparison, in MBHSP02 and MBHSP03 during magnet training are plotted in

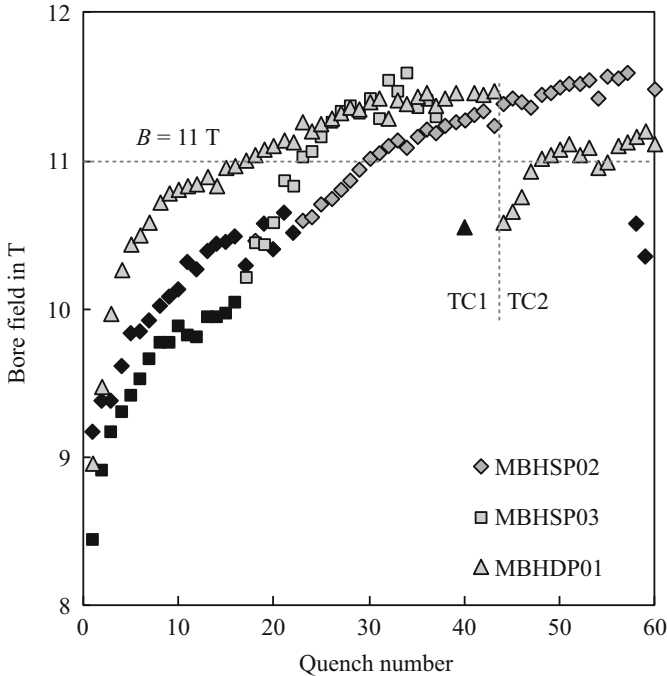


Fig. 8.15 Quench bore field during magnet training. The data at 4.5 K and 1.9 K are represented with filled and non-filled markers, respectively

Fig. 8.15. The bore field was calculated using the measured quench currents and the magnet TFs. The first low-current quenches and the quenches at the highest currents occurred in the IL blocks of coil 7 and coil 10 (the same location and same coils as in the corresponding single-aperture models). The training curve exhibits two regions: the first region with faster training rates, and the second with slower training rates.

The first quench in twin-aperture MBHDP01 occurred at a bore field of ~ 9 T, as in the single-aperture dipole models. A maximum bore field of 11.5 T was reached at a current of 12.1 kA, which is only 0.1 T lower than for the single-aperture models. It can be seen that MBHDP01 training slowed down but still continued.

MBHDP01 training in TC2 started $\sim 9\%$ lower than the maximum bore field achieved in TC1. Magnet re-training was also rather long; after 17 quenches the magnet still quenched below the bore field level reached in TC1. Most of the training quenches in TC2 occurred in coil 10, although each of the four coils quenched at least once, typically at the same locations as in TC1, around the IL middle wedges. The data from the voltage taps and the quench antenna also indicate that the training quenches started near the body-end transition regions.

The ramp-rate dependencies of the MBHDP01 and MBHSP02 bore fields at 1.9 and 4.5 K are plotted in Fig. 8.16. There is a very good correlation of the data at ramp

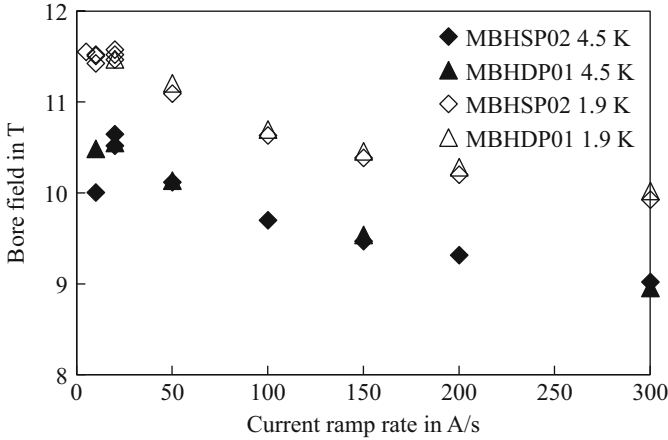


Fig. 8.16 Ramp rate dependence of quench bore field. The data at 4.5 K and 1.9 K are represented with filled and non-filled markers respectively

rates above 20 A/s at both temperatures. All ramp-rate quenches in MBHSP02 and MBHDP01 started in coil 7 at the same location as the training quenches. A relatively low ramp-rate sensitivity of the magnet quench current is due to the use of cables with a stainless-steel core, which suppresses the inter-layer eddy currents in the cable.

Quenches at ramp rates below 20 A/s indicate that the magnet training was not completed at 1.9 K or that the magnet performance was limited by some other effects, for example the current redistribution. The shape of the ramp-rate dependencies at high current ramp rates points to a non-uniform current distribution in the cable, which is also consistent with the axial harmonics variations observed in MBHSP03. Extrapolation of the ramp-rate curves at high ramp rates to zero gives a $B_{\max} \sim 11$ T at 4.5 K and 12 T at 1.9 K.

Temperature dependencies of the quench bore field in twin-aperture MBHDP01 and single-aperture MBHSP02, measured in the temperature range 1.9–4.6 K, are shown in Fig. 8.17. There is a very good correlation between the data for both dipole models at all measured temperatures.

8.3.2.2 Magnetic Measurements

Magnetic measurements were performed in all MBH models using two 16-layer rotating coil probes manufactured with printed circuit board (PCB) technology (DiMarco et al. 2013). In MBHDP01 the coils were placed in the aperture with coils 9 and 10 used in MBHSP03. The measurement data were compared with magnetic measurements in the corresponding single-aperture model MBHSP03 and calculations (Strauss et al. 2016). Figure 8.18 shows the TF for both dipole

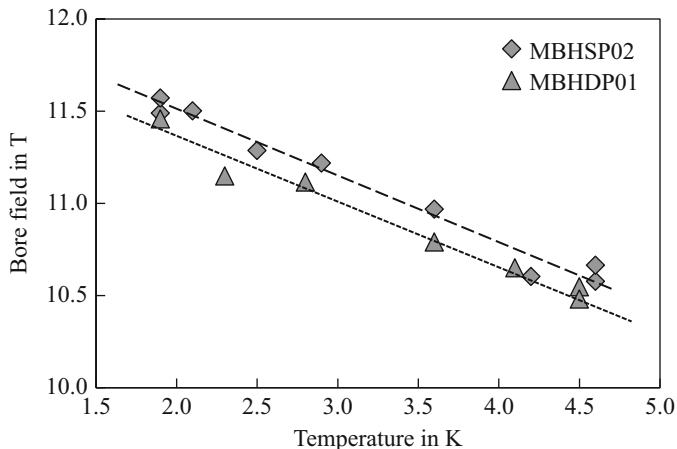


Fig. 8.17 Temperature dependence of the quench bore field in twin-aperture MBHDP01 and single-aperture MBHSP02

models. Figure 8.19 presents the evolution of b_2 and b_3 at $R_{\text{ref}} = 17$ mm vs. the magnet current at a current ramp rate of 20 A/s with a reset current of 100 A.

The iron saturation effect in the TF and b_3 at currents above 4 kA is, in general, consistent with calculations based on iron's magnetic properties and geometry (see Table 8.2). At high currents the difference between calculated and measured TF is less than 1.5%, and the difference for b_3 is less than 6 units. As expected, unlike the single-aperture dipole, the twin-aperture dipole has slightly smaller effects from iron saturation in the TF and b_3 , whereas b_2 is significantly affected due to the aperture cross-talk.

The persistent current effect in the TF and b_3 is substantial in both models at low currents due to the large superconducting filament size and the high critical current density of the Nb₃Sn RRP wires used in both models (see Table 8.4). The ramp-rate effect is small, as expected for a cable with a resistive core.

There is a quite good correlation of the measured and calculated data for the persistent current effect in the TF and b_3 at currents above 1.5 kA when the coil re-magnetization is practically complete, whereas at lower currents there are large discrepancies (Andreev et al. 2013). Therefore, the coil magnetization effect at low currents was studied experimentally at various reset currents in the pre-cycle. The results are shown in Fig. 8.20.

The studies have shown that, due to the relatively long re-magnetization of the Nb₃Sn coils, b_3 at the LHC injection field strongly depends on the reset current. For the Nb₃Sn wires used in the MBH models and a reset current below 100 A, however, this process is practically complete prior to reaching the LHC injection current. It significantly simplifies b_3 correction in the 11 T Nb₃Sn dipoles at injection and at the beginning of acceleration. With the present reset current in the LHC of 100 A, RRP108/127 wire can be used in production magnets for the LHC collimation system upgrade.

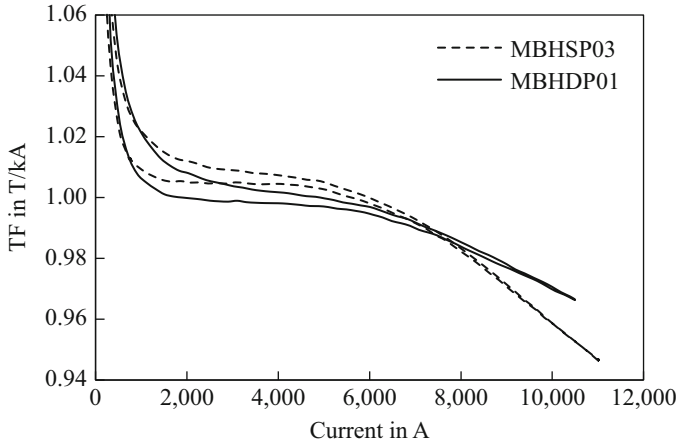


Fig. 8.18 Transfer function vs. current in single- and twin-aperture models

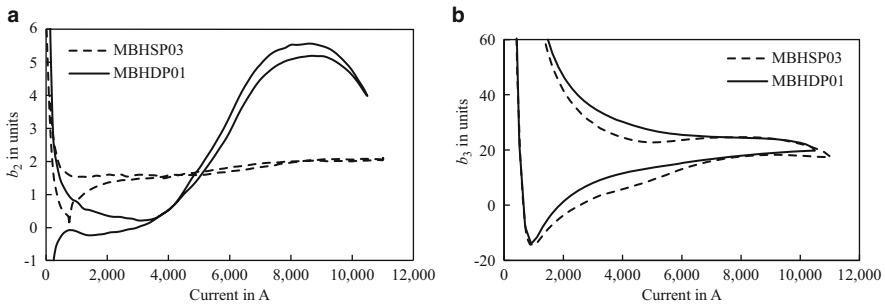


Fig. 8.19 (a) b_2 and (b) b_3 vs. current in single- and twin-aperture models

The b_3 decay was measured in all short models at an LHC injection current of 760 A. It is shown for various reset currents for MBHDP01 in Fig. 8.20. In all the 1 m long magnets, the b_3 decay is reproducible and quite large, within 4–7 units, unlike for the 2 m long MBHSP01 (Andreev et al. 2013) and previously tested Nb₃Sn dipoles (Barzi et al. 2002). The cause of the unexpectedly large b_3 decay in some MBH dipole models remains unknown. One possible explanation could be local core damage (e.g., in the coil ends where the cable experiences large and complex bending deformations), which leads to a local decrease of the inter-strand resistance in these areas.

Axial variations of the normal b_2 and skew a_2 quadrupole components were measured in MBHSP03 using a 26 mm long probe at a magnet current of 6 kA. The harmonic variations shown in Fig. 8.21 had a period comparable to the cable transposition pitch. This periodic variation may indicate a non-uniform current distribution in the cable cross-section, which could also be the cause of the large degradation of the magnet quench currents observed in the models discussed.

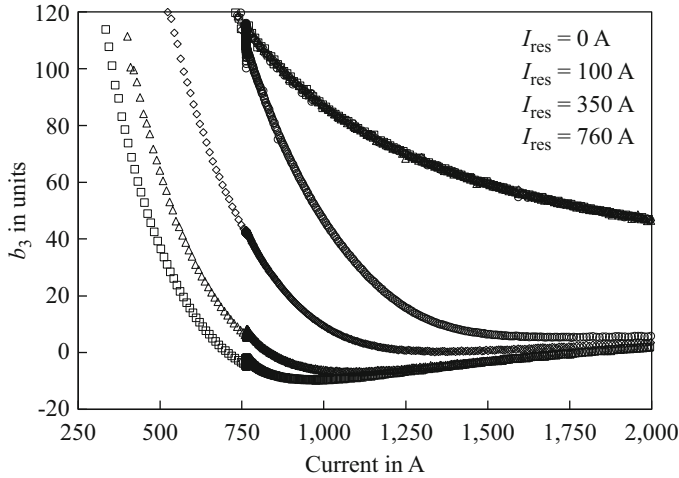


Fig. 8.20 Variations of b_3 at low currents at various reset currents I_{res} in the pre-cycle measured in MBHDP01

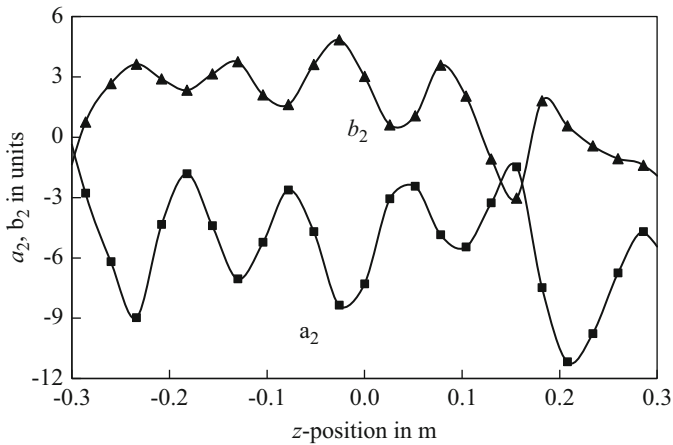


Fig. 8.21 Axial variations of b_2 and a_2 in MBHSP03

The geometrical harmonics at a magnet current of 3.5 kA for the single-aperture and twin-aperture models are summarized in Table 8.8. The resolution of the measurements is better than 0.5 units. The higher order harmonics ($n > 3$) in all of the models are small except for b_9 , which is slightly larger than 1 unit in MBHSP03 and MBHDP01. On the other hand, shimming variations in the models to achieve the target pre-stress levels give rise to sizable differences in the lower-order harmonics.

Table 8.8 Field harmonics at $I = 3.5$ kA

n	MBHSP02		MBHSP03		MBHDP01	
	a_n	b_n	a_n	b_n	a_n	b_n
2	0.1	-4.9	-4.6	1.4	-3.5	0.6
3	-1.4	8.4	2.0	16.1	0.4	20.9
4	0.2	-0.2	-0.1	0.1	0.3	0.3
5	0.2	1.0	-0.1	0.8	-0.5	-0.2
6	0.0	-0.2	-0.3	-0.2	-0.1	0.4
7	-0.1	0.0	0.0	0.3	-0.5	-0.2
8	0.0	0.0	0.1	0.0	0.1	0.2
9	0.1	0.2	0.2	1.3	0.5	1.1

8.3.2.3 Quench Protection Studies

The quench protection problem of the 11 T dipoles was comprehensively studied at FNAL, including simulations and measurements of short dipole and dipole mirror models (Chlachidze et al. 2013a, b; Zlobin et al. 2012b, 2014). In dipole mirror MBHSM01 spot heaters made of stainless-steel strip were mounted on the IL and OL mid-plane turns of coil 8. Each spot heater was surrounded by two voltage taps. Two additional voltage taps, separated by 10 cm, were also installed next to the spot heater. Due to the damage to the IL spot heater wiring during magnet assembly, studies were only performed with the OL spot heater.

Quench Temperature Measurements

The coil maximum temperature after a quench is estimated based on the quench integral (QI) calculated over the current decay time using the adiabatic approach (see Chap. 1), and usually represented in MIITs ($1 \text{ MIIT} = 10^6 \text{ A}^2\text{s}$). Simulations of quench processes show that heat transfer from the quenched cable inside the magnet coil plays an important role. To study the effect of heat transfer from the cable, the cable temperature growth in the coil due to a quench was measured using quenches induced by the spot heater at fixed coil current. The temperature of the cable in coil was estimated using the known dependence of the copper matrix resistivity on the temperature and magnetic field.

The measured cable temperature vs. the time after quench at constant coil currents is plotted in Fig. 8.22. The dashed lines connect the temperature points corresponding to the same QI values. The temperature points on the vertical axis ($t = 0$) represent the adiabatic calculations for the corresponding bare cable. It can be seen that the cable temperature depends not only on the value of QI , but also on the time during which it is accumulated, which is consistent with efficient heat transfer from the quenched cable. Since the quench time of an accelerator magnet is usually longer than 0.2 s, traditional adiabatic calculations significantly overestimate the coil temperature after quench.

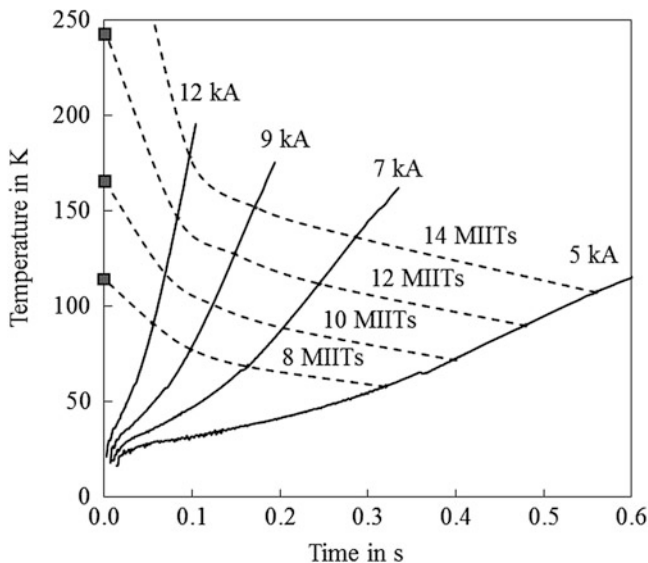


Fig. 8.22 Cable temperature after quench vs. time measured at various currents in coil (MBHSM01)

Longitudinal Quench Propagation Velocity

The quench propagation velocity along the cable in a coil is an important parameter for estimating the QI in the area of quench origin and for optimizing the protection heater design. The quench propagation velocity in the OL mid-plane turn was measured using the spot heater. The quench propagation velocity along the cable was determined using the slope of $V(t)$ dependence between the voltage taps next to the spot heater (method A), and the measured quench propagation time and the known distance between the two voltage taps (method B). The quench propagation velocity in the IL pole turn was estimated using the dV/dt slope during some training quenches. The measured data for the OL mid-plane turn and the IL pole turn are shown in Fig. 8.23. The experimental data in Fig. 8.23 are in agreement with calculations. These data provide an important input for the optimization of the quench detection voltage threshold and the signal discrimination time.

Radial Quench Propagation

Simulations and heater studies in 11 T dipole models revealed that a quench propagates quite rapidly in the radial direction from OL to IL coil blocks. It helps to distribute the magnet's stored energy over a larger coil volume and, thus, to reduce the coil maximum temperature. The quench delay time (the time between heater initiation and coil quench) was measured separately for the coil OL and IL blocks at 4.5 K and 1.9 K. The quench propagation time between the coil layers was estimated

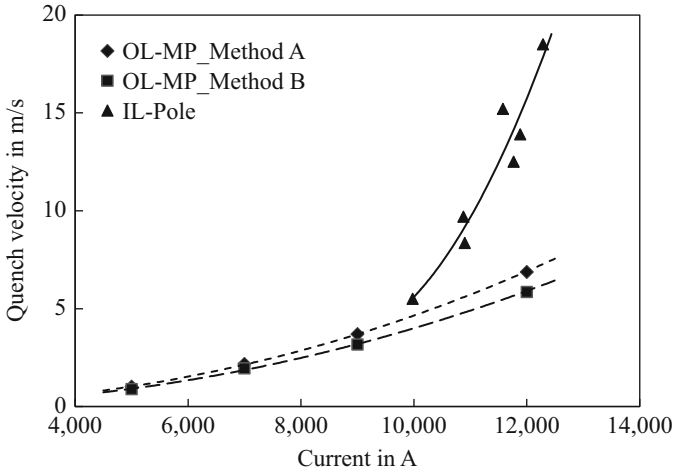


Fig. 8.23 Longitudinal quench velocity in coil (MBHSM01). MP, mid-plane; OL, outer layer; IL, inner layer

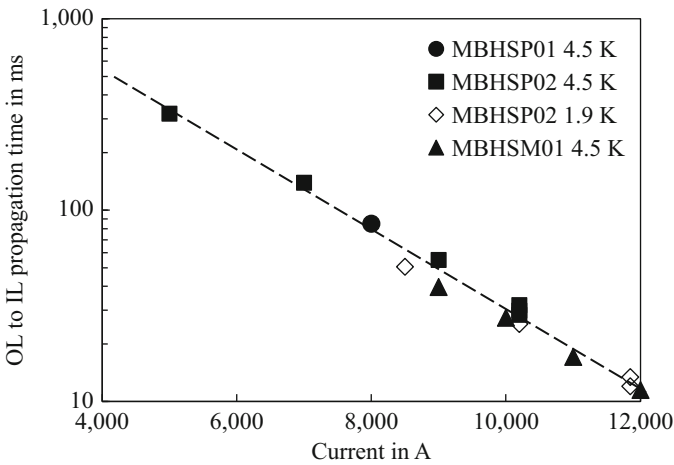


Fig. 8.24 Radial quench propagation time from outer layer to inner layer

as the time difference between the detection of a quench in the OL and IL of the coil. Figure 8.24 shows this time difference vs. the magnet current. Similar results for different coils in different magnets confirm the excellent reproducibility of this effect in Nb₃Sn coils. At currents close to the LHC nominal operating current the radial quench propagation time is smaller than 20 ms. It means that, after a heater-induced quench, the coil OL serves as an efficient quench heater for the IL coil.

8.4 FNAL 11 T Dipole R&D Summary

Dipole models with a field strength of 11 T for the LHC upgrade have been developed, fabricated, and tested at FNAL. Two single-aperture and twin-aperture models were trained to bore fields of 11.5–11.7 T, which are close to the magnet design field of 12 T. It demonstrated the viability of the magnet design and technology developed. At this point FNAL's part in the joint 11 T dipole R&D program for the LHC upgrade was completed. Some open questions, however, remain. The most important open questions are the observed long magnet training and noticeable re-training, large conductor degradation, and the non-uniform current distribution in the Rutherford cables in the magnet coils. The latter could be a cause of the spontaneous quenches at a current plateau observed in some models. These issues need to be further understood and addressed.

References

- Andreev N, Barzi E, Chichili DR et al (2002) Volume expansion of strands and cables during heat treatment. *Adv Cryo Eng* 48(614):941–948. <https://doi.org/10.1063/1.1472635>
- Andreev N, Apollinari G, Barzi E et al (2013) Field quality measurements in a single-aperture 11 T Nb₃Sn demonstrator dipole for LHC upgrades. *IEEE Trans Appl Supercond* 23(3):4001804. <https://doi.org/10.1109/TASC.2013.2237819>
- Auchmann B, Karppinen M, Kashikhin VV et al (2012) Magnetic analysis of a single-aperture 11 T Nb₃Sn demonstrator dipole for LHC upgrades. In: *Proceedings of 2012 international particle accelerator conference, New Orleans, May 2012*, p 3596
- Barzi E, Carcagno R, Chichili D et al (2002) Field quality of the Fermilab Nb₃Sn cos-theta dipole models. In: *Proceedings of 2002 European particle accelerator conference, Paris*, p 2403
- Barzi E, Karppinen M, Lombardo V et al (2012) Development and fabrication of Nb₃Sn Rutherford cable for the 11 T DS dipole demonstration model. *IEEE Trans Appl Supercond* 22(3):6000805. <https://doi.org/10.1109/TASC.2011.2180869>
- Bossert RC, Andreev N, Chlachidze G et al (2011) Fabrication and test of 90-mm Nb₃Sn model based on dipole type collar. *IEEE Trans Appl Supercond* 21(3):1777–1780. <https://doi.org/10.1109/TASC.2010.2089418>
- Bottura L, de Rijk G, Rossi L et al (2012) Advanced accelerator magnets for upgrading the LHC. *IEEE Trans Appl Supercond* 22(3):4002008
- Chlachidze G, Novitski I, Zlobin AV et al (2013a) Experimental results and analysis from 11 T Nb₃Sn DS dipole. FERMILAB-CONF-13-084-TD, and WAMSDO'2013, CERN-2013-006, CERN, Geneva
- Chlachidze G, Andreev N, Apollinari G et al (2013b) Quench protection study of a single-aperture 11 T Nb₃Sn demonstrator dipole for LHC upgrades. *IEEE Trans Appl Supercond* 23(3):4001205. <https://dx.doi.org/10.1109/TASC.2013.2237871>
- de Rijk G, Milanese A, Todesco E (2010) 11 Tesla Nb₃Sn dipoles for phase II collimation in the Large Hadron Collider. sLHC Project Note 0019, CERN, Geneva
- DiMarco J, Chlachidze G, Makulski A et al (2013) Application of PCB and FDM technologies to magnetic measurement probe system development. *IEEE Trans Appl Supercond* 23(3):9000505. <https://doi.org/10.1109/TASC.2012.2236596>
- Karppinen M, Andreev N, Apollinari G et al (2012) Design of 11 T twin-aperture Nb₃Sn dipole demonstrator magnet for LHC upgrades. *IEEE Trans Appl Supercond* 22(3):4901504, <https://doi.org/10.1109/TASC.2011.2177625>
- Russenschuck S (1995) A computer program for the design of superconducting accelerator magnets. CERN AC/95–05 (MA), September 1995, CERN, Geneva

- Strauss T, Apollinari G, Barzi E et al (2016) Field quality measurements in the FNAL twin-aperture 11 T dipole for LHC upgrades. In: Proceedings of 2016 North American particle accelerator conference, Chicago, 9–14 October 2016, p 158
- Zlobin AV (2010) Status of Nb₃Sn accelerator magnet R&D at Fermilab. In: EuCARD – HE-LHC’10 AccNet mini-workshop on a High-Energy LHC, 14–16 October 2010, CERN Yellow Report CERN-2011-003, p 50 [arXiv:1108.1869], CERN, Geneva
- Zlobin AV, Andreev N, Apollinari G et al (2011) Development of Nb₃Sn 11 T single aperture demonstrator dipole for LHC upgrades. In: Proceedings of 2011 particle accelerator conference, New York, March 2011, p 1460
- Zlobin AV, Andreev N, Apollinari G et al (2012a) Design and fabrication of a single-aperture 11 T Nb₃Sn dipole model for LHC upgrades. IEEE Trans Appl Supercond 22(3):4001705. <https://doi.org/10.1109/TASC.2011.2177619>
- Zlobin AV, Novitski I, Yamada R (2012b) Quench protection analysis of a single-aperture 11 T Nb₃Sn demonstrator dipole for LHC upgrades. In: Proceedings of 2012 International particle accelerator conference, New Orleans, May 2012, p 3599
- Zlobin AV, Andreev N, Apollinari G et al (2013) Development and test of a single-aperture 11T Nb₃Sn demonstrator dipole for LHC upgrades. IEEE Trans Appl Supercond 23(3):4000904. <https://doi.org/10.1109/TASC.2012.2236138>
- Zlobin AV, Chlachidze G, Nobrega F et al (2014) Quench protection studies of 11 T Nb₃Sn dipole coils. In: Proceedings of 2014 international particle accelerator conference, Dresden, 15–20 June 2014, p 2725

Open Access This chapter is licensed under the terms of the Creative Commons Attribution 4.0 International License (<http://creativecommons.org/licenses/by/4.0/>), which permits use, sharing, adaptation, distribution and reproduction in any medium or format, as long as you give appropriate credit to the original author(s) and the source, provide a link to the Creative Commons licence and indicate if changes were made.

The images or other third party material in this chapter are included in the chapter’s Creative Commons licence, unless indicated otherwise in a credit line to the material. If material is not included in the chapter’s Creative Commons licence and your intended use is not permitted by statutory regulation or exceeds the permitted use, you will need to obtain permission directly from the copyright holder.

